INSTITUTE OF PHYSICS PUBLISHING PHYSICS IN MEDICINE AND BIOLOGY

Phys. Med. Biol. **46** (2001) 1785–1798 www.iop.org/Journals/pb PII: S0031-9155(01)21837-5

Comparison of modelled and observed *in vivo* temperature elevations induced by focused ultrasound: implications for treatment planning

Kathleen Mahoney, Todd Fjield[1], Nathan McDannold, Greg Clement and Kullervo Hynynen

Department of Radiology, Brigham and Women's Hospital and Harvard Medical School, 221 Longwood Avenue, Room 013, Boston, MA 02115, USA

Received 9 February 2001, in final form 11 April 2001

Abstract

Two numerical models for predicting the temperature elevations resulting from focused ultrasound heating of muscle tissue were tested against experimental data. Both models use the Rayleigh–Sommerfeld integral to calculate the pressure field from a source distribution. The first method assumes a source distribution derived from a uniformly radiating transducer whereas the second uses a source distribution obtained by numerically projecting pressure field measurements from an area near the focus backward toward the transducer surface. Both of these calculated ultrasound fields were used as heat sources in the bioheat equation to calculate the temperature elevation *in vivo*. Experimental results were obtained from *in vivo* rabbit experiments using eight-element sector-vortex transducers at 1.61 and 1.7 MHz and noninvasive temperature mapping with MRI. Results showed that the uniformly radiating transducer model over-predicted the peak temperature by a factor ranging from 1.4 to 2.8, depending on the operating mode. Simulations run using the back-projected sources were much closer to experimental values, ranging from 1.0 to 1.7 times the experimental results, again varying with mode. Thus, a significant improvement in the treatment planning can be obtained by using actual measured ultrasound field distributions in combination with backward projection.

(Some figures in this article are in colour only in the electronic version; see `www.iop.org`)

1. Introduction

Modelling of the thermal fields produced by ultrasound in tissue is important both in the area of diagnostic ultrasound, where it can aid in establishing safety levels, and in the rapidly growing field of focused ultrasound (FUS) surgery, where it is used for treatment planning and establishing safety thresholds. In FUS surgery, the goal is to heat a small tissue volume above

[1] Currently at Transurgical, Inc., 220 Belle Meade Road, Setauket, NY 11733, USA.

0031-9155/01/071785+14$30.00

the threshold for coagulation (∼60 °C) while remaining below the boiling point, in order to destroy the targeted tissue without incurring the negative affects associated with boiling. To date, there is a substantial body of work on acoustic field simulations of therapeutic transducers (for example Robinson and Lele 1972, Carstensen *et al* 1981, Lizzi *et al* 1984, Swindell *et al* 1982, Nyborg 1981, Clarke and ter Haar 1997, Fan and Hynynen 1995, Fan *et al* 1997) and the resulting temperature distributions (for example Carstensen *et al* 1981, Billard *et al* 1990, Lin *et al* 1992) and lesion volumes (Robinson and Lele 1972, Lizzi *et al* 1984, Hill *et al* 1994, Damianou *et al* 1995, Meaney *et al* 1998). Experimental verification of these models has been only in terms of histological inspections of the resulting lesion shape/extent. However, no studies testing the actual temperature prediction have been made. Moreover, the previous studies used single element transducers that have very sharp gradients in the acoustic and corresponding temperature fields. Thus the volumes of the coagulated tissue created by such transducers are not very sensitive to the accuracy of the temperature prediction. Phased array transducers are used to produce larger focal areas and can coagulate large volumes with their flatter temperature distributions. These focal areas are created by more complicated acoustic fields such a scanned single focus, multiple foci or a combination of focal patterns. While these arrays provide enormous potential benefits in terms of reduced treatment times and the possibility of electrical steering of the field, they are also more complex to control. The high power levels required for the large focal areas also deposit more energy in the tissue per sonication over a larger volume, increasing the thermal effects in front of the focal volume. The manipulation of the acoustic field may make it more difficult to determine the required power level needed for a given sonication based on experimental study alone. For example, if the focus is electronically steered, the energy deposition can be different for each sonication. (Electrical steering is advantageous because it allows for significant space saving in the positioning system along the dimension at which space is at a premium, as well as reducing the number of moving parts.) Therefore, mathematical models for predicting the temperature elevation are required so that the sonication parameters can be determined for an FUS treatment. In this study the *in vivo* temperature distributions induced by phased array ultrasound applicators were compared with predicted temperature distributions. In addition a new method that allows the measured properties of a specific transducer to be utilized to improve the prediction was compared to simulations of the ultrasound field.

2. Methods and materials

2.1. Ultrasound

Two in-house constructed eight-element, spherically curved sector transducers (for the basic principles see the article by Cain and Umemura (1986)) were used for the *in vivo* experiments. Both arrays were made from a spherically curved lead zirconate titanate shell. Figure 1 shows a schematic diagram of the transducer geometry. The kerfs between the elements were filled with silicon rubber to maintain spherical alignment. The ceramic shell was mounted in a polycarbonate holder with an air space behind the array. The transducer elements were individually impedance matched to 50 Ω at the desired operating frequency to give them the greatest efficiency. The transducers had an operating frequencies of 1.61 MHz and 1.7 MHz.

The RF power and phase supplied to each array element could be independently controlled by an in house manufactured multi-channel amplifier system. This system has eight bits of power control and better than 1° of phase resolution at 1.5 MHz (Daum *et al* 1998). The operating 'mode' of the transducer indicates the number of the times the phase of the elements varies by 2π moving around the circumference of the transducer. Because the difference in

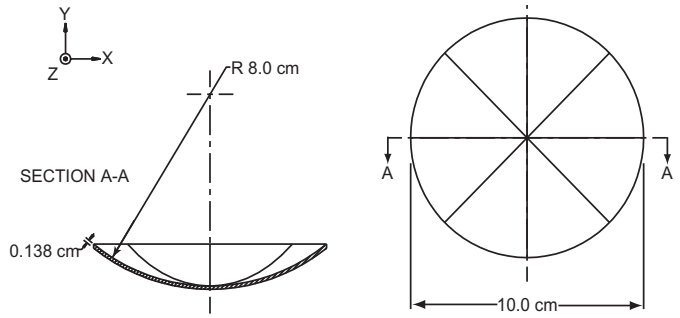

Figure 1. Diagram of the geometry of a spherically curved sector vortex transducer. On the right side is a top view of the transducer showing the eight sectors.

phase between adjacent elements must be equal for a circular (symmetric) focus, the maximum mode that can be obtained with eight elements is mode 4. This corresponds to neighbouring elements being 180° out of phase. The phases for the elements of a sector vortex array are calculated as

$$\theta_n = mn\left(\frac{2\pi}{N}\right)$$

where m is the mode number, θ_n is the phase of sector $n = 0, 1, \ldots, N-1$, $m \leqslant N/2$ is the mode of phase revolution (when $m = 0$, the transducer reduces to a geometrically focused transducer) and N is the total number of sectors in the array (Cain and Umemura 1986). For an eight-sector array, modes higher than mode 0 produce a ring of eight focal points (one per sector). The resulting acoustic field shape of the spherically curved sector-vortex array has a shape determined by the mth order Bessel function. The radius of the annular focal region is roughly proportional to the vortex mode m (Cain and Umemura 1986). Thermal conduction fills in the centre of this ring, and so higher modes produce lesions with the same familiar 'grain of rice' shape as a single focus transducer, but with a larger diameter.

2.2. Acoustic field measurements

The acoustic fields were characterized in degassed water. Stepper motors scanned a 0.2 mm diameter needle hydrophone (Precision Acoustics, UK) across a plane in the focal region of the transducer (perpendicular to the direction of the ultrasound beam). Both transducers were scanned in modes 0 and 4. Mode 0 scans were performed at 2 W (electrical power, or ∼1.4 W acoustic) and mode 4 scans were performed at 4 W (∼2.8 W acoustic). The scan area was 100 mm^2 with a 0.2 mm step size. Both magnitude and phase information was recorded at each point to allow back propagation of the wave front (Clement *et al* 1998). The total acoustic power as a function of RF power was measured using a radiation force measurement system. The RF power (forward and reflected) and driving phase was monitored during each sonication by power meters integrated into the amplifier system (manufactured in house). The transducer efficiencies were 70% and 71% for the 1.61 MHz and 1.7 MHz, respectively.

2.3. Acoustic field and temperature simulations

The acoustic pressure fields were calculated using a numerical method of summation of simple sources as described by Zemanek (1971): the surface of the transducer may be modelled as a collection of point sources and the pressure at each point, p, in a region of interest is

obtained from the velocity potential Ψ_p at that point. The velocity potential can be calculated by summing the contributions from each point source, a, using the Rayleigh–Sommerfeld integral:

$$\overline{\Psi_p} = \int\int_A \frac{u_a}{2\pi r_{ap}} \mathrm{e}^{-\mathrm{i}kr_{ap}} \mathrm{e}^{-\sum \mu_i r_{ap,i}}$$

where k is the wave number, u_a is the normal velocity of the point source, r_{ap} is the distance from source a to point p, $r_{ap,i}$ is the portion of the path from source a to point p in medium i and μ_i is the attenuation in medium i.

In the traditional uniformly radiating model, the surface of the transducer is assumed to uniformly radiate acoustic energy. The surface is divided up into area elements (possibly of differing sizes), and the strength of each source is proportional to the element area and the total emitted power of the transducer. In other words, the power per unit area emitted by the transducer is the same throughout the transducer surface. In reality, this is not the case. Transducer elements may radiate much better near their centres than at the edges. A transducer with many elements will radiate unevenly, and the exact nature of this nonuniformity will depend on difficult-to-model details of the construction. By scanning through a small planar region across the whole ultrasound field at low acoustic power (2–4 W) and recording both the magnitude and phase of the pressure, we can obtain a 'fingerprint' of the transducer. Using harmonic projection methods (Clement and Hynynen 2000), this information can be used to determine the magnitude and phase of the pressure field at each point in another plane, such as a flat plane at the top surface of the transducer. If we assume the acoustic field satisfies the linearized acoustic wave equation, we may separate out harmonic time dependence and express the pressure as $P(r, t) = \tilde{P}(r)\,\mathrm{e}^{\mathrm{i}\omega t}$. Using a 2D Fourier integral substitution, the wave equation can be converted to a Cartesian Helmholtz equation. In wave vector space, the projection algorithm relating the measured field at a plane z_0 to that at another plane z, obtained from a solution to this Helmholtz equation, is (Clement and Hynynen 2000)

$$\tilde{p}(k_x, k_y, z) = \tilde{p}(k_x, k_y, z_0)\,\mathrm{e}^{\mathrm{i}(z-z_0)\sqrt{(\omega^2/c^2)-k_x^2-k_y^2}}.$$

The pressure field in real space is obtained by an inverse transform. In the simulations that used the harmonic back-projection method, this was how the simple sources were calculated. The magnitudes were scaled linearly with power to yield the source distribution for the Rayleigh–Sommerfeld equation.

Pressure field calculations were fully 3D and included the effects of tissue layers (e.g. a skin layer with different acoustic properties could be included) and attenuation from different focal depths. The spatial resolution of the pressure field was 0.25 mm × 0.25 mm × 0.5 mm. The calculated pressure field was considered to exist during the entire duration of the pulse and essentially acts as a source term in the bioheat equation. The temperature field was likewise treated as fully 3D, although the symmetries about the x and y axes were employed to decrease calculation time.

The temperature field was calculated using the Pennes bioheat equation (Pennes 1948) without considering nonlinear contributions which should be small with the sharply focused transducers used (Swindell *et al* 1982, Hynynen 1991):

$$\rho_{\mathrm{tissue}} c_{\mathrm{tissue}} \frac{\mathrm{d}T}{\mathrm{d}t} = k_{\mathrm{kissue}} \nabla^2 T - \omega c_{\mathrm{blood}} (T - T_{\mathrm{blood}}) + \langle q \rangle.$$

The $\langle q \rangle$ term is the heat source produced by the ultrasound field. The parameters used for simulating the pressure and temperature fields are shown in table 1. The skin layer thickness was chosen to be 2 mm based on measurements from both MRI sections and a sample of rabbit thigh skin. Simulations were performed initially with a source distribution on the surface

Table 1. Parameters used in simulating the pressure field and temperature elevations. The skin layer was assumed to be 2.0 mm thick based on measurements of tissue samples. Parameter values chosen from data summarized by Hynynen (1990). When a range of values was available, a median value was chosen.

	Value in			
Parameter	Water	Skin	Muscle	Units
ρ_t—tissue density	998	1200	1170[a]	kg m^{-3}
α—attenuation coefficient[b]	0.0	40[c]	4.1[d]	Np m^{-1} MHz^{-1}
v_c—sound speed	1500	1498	1570[e]	W m^{-1} °C^{-1}
c_b—specific heat of blood	—	3770	3770	J kg^{-1} °C^{-1}
c_t—specific heat of tissue	4178	3770	3770	J kg^{-1} °C^{-1}
k_t—tissue thermal conductivity	0.628	0.5	0.5	W m^{-1} °C^{-1}
ω_b—blood perfusion rate	0.0	1	1	kg m^{-3} s^{-1}

[a] Range 1070–1270.
[b] Also absorption coefficient.
[c] Range 14–66.
[d] Range 2.6–8.8.
[e] Range 1508–1630.

of the transducer corresponding to a uniformly radiating surface. Additional simulations of modes 0 and 4 were performed using a source distribution generated from hydrophone scans of the transducer focus which was then back propagated to the plane of the transducer face using a harmonic projection method. Temperature fields were simulated for the frequencies, modes, acoustic powers and pulse durations used in the experiments. Because tissue is a lossy medium, the depth into the tissue of the focal point will also affect the temperature field. Depths for experimental data ranged from 1.0 to 3.0 cm from the surface of the skin. Temperature values for each mode were obtained by performing simulations at depths corresponding to the measured depths of each experimental temperature point and averaging them. Simulations were also performed with and without the 2 mm skin layer.

2.4. Averaging over voxel volume

The size of a voxel (volume element) in the MR images used in this study was $0.625 \times 0.625 \times 3.0$ mm^3. The temperature measurement registered for an individual voxel element was an average of the temperature of the tissue contained in the volume element. Therefore, the maximum temperature obtained from MR imaging was less than the maximum temperature of the tissue. The results from the simulations reported temperature values at specific points in the temperature field, in this case, at points every 0.25 mm in x and y and every 0.5 mm in z. Because it was not possible to reconstruct the exact temperature field distribution from the MR images, the simulated distributions were instead averaged over a volume element. In the radial (xy or r) plane, averages were taken with the hottest point in different positions within a voxel, ranging from dead centre (producing the highest average temperature) to far off into one corner of the voxel. Assuming all positions to be equally likely, mean and standard deviation for the average temperatures were obtained. Temperature varies more slowly with distance along the transducer axis (z direction), and the location of the imaging plane can be measured accurately. Therefore, the effects of shifting the position of the focus axially were small enough compared to the effects of shifting it radially that only results for z-centred voxel averaging are shown.

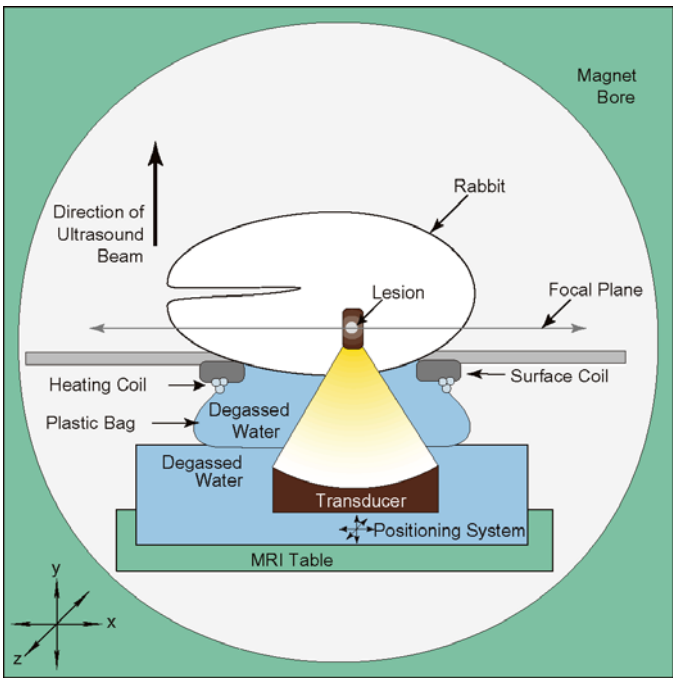

Figure 2. Illustration of the experimental setup for the *in vivo* sonications in rabbit thigh.

2.5. MRI monitored in in vivo experiments

Two sets of *in vivo* animal experiments were performed, in which the skeletal thigh muscles of New Zealand white rabbits (3–4 kg) were sonicated. The rabbits' thighs were shaved with clippers, and any remaining hair was removed with depilatory cream. The rabbits were anaesthetized with a mixture of 40 mg kg^{-1} ketamine (Aveco Co., Inc., Fort Dodge, IA) and 10 mg kg^{-1} xylazine (Lloyd Laboratories, Shenandoah, IA) and placed on a three-axis positioning system (GE Medical Systems, Milwaukee, WI). An open plastic bag filled with deionized, degassed water was used to acoustically couple the transducer to the surface of the animal. A 12.5 cm diameter receive-only imaging coil was placed under the animal around the plastic bag to improve image quality. The positioning system was placed in the bore of a standard 1.5 T clinical MRI scanner (Signa, GE Medical Systems). Figure 2 illustrates this experimental setup. The rabbit's body temperature was monitored by a rectal thermocouple. During the second set of experiments (with the 1.7 MHz transducer), the water in the water bag was heated by a coil of warm water around the bag, to ensure more uniform body temperature in the thigh muscle.

In the first experiments, the 1.61 MHz transducer was used to deliver a total of 30 10 second sonications in different modes into the thighs of a total of seven rabbits. All five modes (0, 1, 2, 3, 4) were used and the power was scaled by mode to produce approximately the same peak temperature. In the second experiments, which used the 1.7 MHz transducer, sonications were made only in modes 0 and 4, but durations of both 10 and 20 seconds were examined, and at each mode, several different powers were used. A total of 105 sonications at separate locations were made in 15 rabbits in this experiment.

Temperature rise above the baseline temperature was measured noninvasively using a fast spoiled gradient-echo (FSPGR) sequence. This sequence estimates the change in the

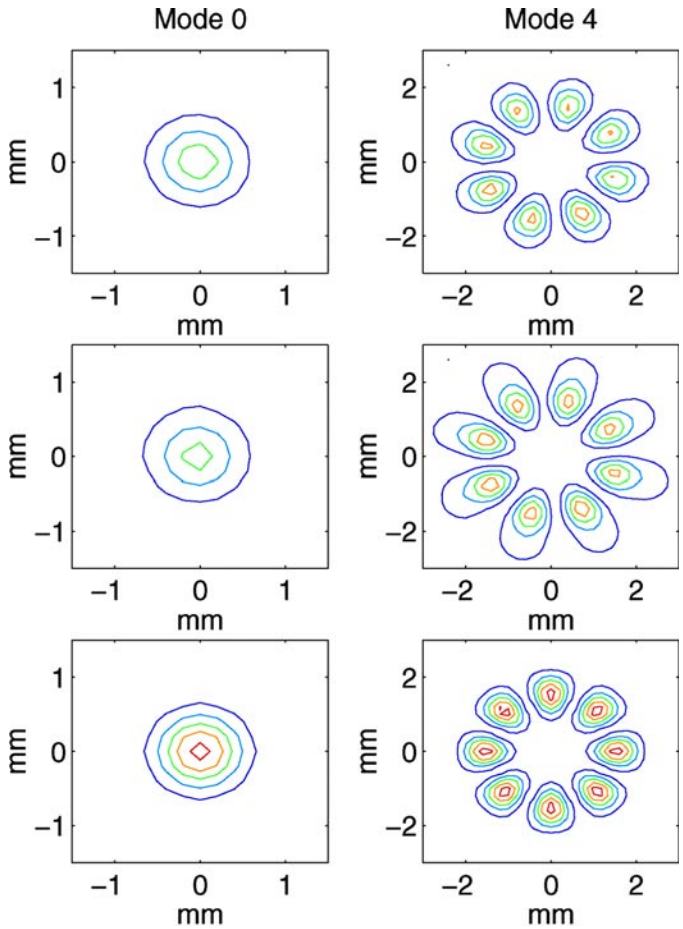

Figure 3. Comparison of the simulated and measured (in water) acoustic field distributions taken through the focus in a plane perpendicular to the transducer's axis of symmetry for modes 0 and 4. The top row shows the measured fields, the middle row shows the simulated field produced by the back-projection method and the bottom row the simulation results produced by the uniformly radiating model. The experimental and back-projected models produce pressure fields that are more smeared out than the uniformly radiating model. The eight spots visible in mode 4 correspond to the eight sectors. Thermal conduction causes the temperatures between the spots to 'fill in' in a few seconds, so higher modes effectively increase the focal volumes. The transducer operating frequency is 1.61 MHz. The lines are contours at 10% intervals.

water proton resonant frequency (PRF) shift, which is linear with temperature in the ranges of these experiments (Kuroda *et al* 1998). The imaging parameters were repetition time (TR) = 26.1 ms, echo time (TE) = 12.8 ms, bandwidth (BW) = 7.2 kHz, flip angle = 30°, field of view (FV) = 160 mm, slice thickness = 3 mm, matrix = 256 × 128, scan time per image = 4 s and number of acquisitions (NEX) = 1 for the first experiment. In the second experiment a more sensitive sequence was used with TR = 40.2 ms, TE = 19.6 ms and BW = 3.57 kHz (remaining parameters the same as previous experiment). Using real and imaginary images from the scanner, phase maps were calculated. Changes in PRF (and thus temperature) were determined by performing complex phase map subtractions; a baseline phase map was acquired prior to the sonication and subsequent phase maps, acquired during

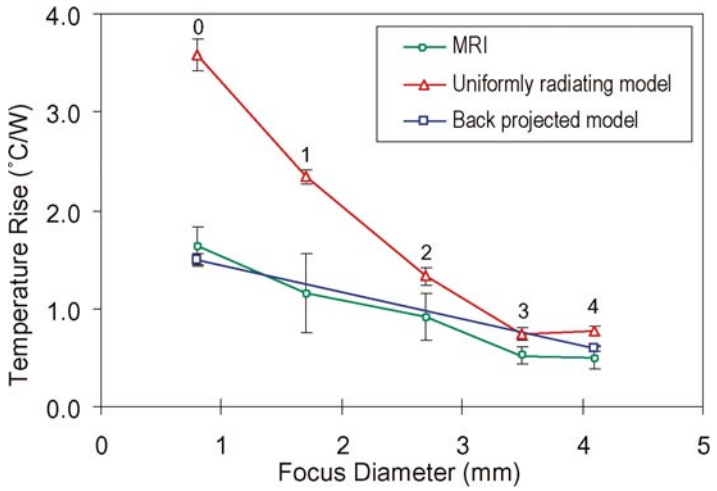

Figure 4. Peak temperature rise (°C) per watt of applied acoustic power is shown by focal diameter for experimental (1.61 MHz transducer) and simulated data. The small numbers above the data indicate the transducer operating mode. Results from MRI are the average of multiple sonications. Simulated results have been voxel averaged to match the resolution of the MRI results. Although the data from the 1.7 MHz transducer is not shown here, it is in good agreement with the shown results for modes 0 and 4 and a 10 second pulse.

the sonication and cooling periods, were subtracted from it (Chung *et al* 1996). The MRI sequence was calibrated in *in vivo* rabbit thigh muscle by Kuroda *et al* (1998). The calibration coefficient of -0.009 ppm $^{\circ}C^{-1}$ of frequency shift was used for these measurements.

3. Results

3.1. Acoustic field measurements

The hydrophone scans of the acoustic intensity distributions produced by the 1.61 MHz sector vortex array operating in modes 0 and 4 are shown in figure 3 (top row) along with the simulated intensity distributions. The simulated fields produced by the harmonic back projection method showed better agreement with the measured fields than those produced assuming a uniformly radiating transducer.

3.2. Temperature prediction experiments

Voxel averaging of the temperature field around the peak temperature was performed and showed a substantial decrease of the expected peak temperature, particularly at the lower modes. For the uniformly radiating transducer model at mode 0, voxel averaging resulted in a 25–30% decrease of the peak temperature value. However simulations still over-predicted the temperature by a factor 2.2 to 2.8, indicating that the averaging effects of the MRI were not the only source of error. At mode 4, voxel averaging yielded a 10–15% decrease, which resulted in a 1.4 to 2.0 over-prediction. For simulations using back-projected sources, the reductions due to voxel averaging were 15–17% for mode 0 and 5–6% for mode 4. As expected, in the absence of a skin layer, the temperature values were much higher. The amount of decrease in peak temperature value with voxel averaging is a measure of how sharply focused the pressure field is; a flatter profile will result in the averaged and unaveraged peak values being closer

Table 2. Temperature rise in degrees per watt of applied acoustic power for lesions produced *in vivo* compared with temperature rise predicted from the two sets of simulations, the first with sources generated by back-projecting pressure field measurements and the second by assuming a uniformly radiating transducer. No simulations were run in modes 1, 2 or 3 with the back-projected sources. Simulated results are the average of multiple simulations at tissue depths corresponding to experimental depths and are also voxel averaged, meaning the results are averaged over a region corresponding to one MRI volume element (voxel). The top portion of the table shows results for the 1.61 MHz transducer and the lower portion shows results for the 1.7 MHz transducer. The ratio listed for each model is the ratio of simulated to experimental temperature rise and hence the over-prediction factor.

					Back-projected model		Uniformly radiating model	
Mode	Pulse length (s)	No of sonic-ations	Acoustic power (W)	Experimental temperature rise ($^\circ$C W^{-1})	Temperature rise ($^\circ$C W^{-1})	Ratio sim./exp.	Temperature rise ($^\circ$C W^{-1})	Ratio sim./exp.
0	10	3	33.0	1.64±0.20	1.50±0.06	0.9	3.58±0.16	2.2
1	10	5	39.4	1.16±0.40	—	—	2.34±0.08	2.0
2	10	5	72.4	0.92±0.25	—	—	1.33±0.09	1.5
3	10	6	93.5	0.52±0.08	—	—	0.75±0.06	1.4
4	10	11	107.5	0.50±0.11	0.59±0.04	1.2	0.77±0.05	1.6
0	10	4	32.1	1.24±0.29	2.12±0.08	1.7	3.48±0.15	2.8
0	20	5	42.8	1.69±0.44	2.41±0.09	1.4	4.39±0.15	2.6
4	10	14	64.3	0.42±0.09	0.68±0.07	1.6	0.73±0.08	1.7
4	10	20	85.6	0.45±0.11	0.71±0.06	1.6	0.76±0.06	1.7
4	10	17	107.1	0.45±0.13	0.69±0.06	1.5	0.74±0.07	1.7
4	20	8	32.1	0.80±0.41	0.96±0.00	1.2	1.19±0.00	1.5
4	20	6	42.8	0.68±0.18	0.94±0.06	1.4	1.17±0.07	1.7
4	20	5	64.3	0.69±0.18	0.94±0.04	1.4	1.18±0.02	1.7

than those for a sharp profile. In addition to the variations with mode, there were also small variations between the simulated and experimental results with duration—predictions for 20 s simulations agreed slightly better with experimental data than for 10 s simulations.

In contrast, the simulations that used the back-projected sources resulted in temperature predictions that were closer to the experimental results. The simulations in mode 0 predicted temperatures that were between 0.9 and 1.7 times the experimentally measured values: less than half the value predicted by the uniformly radiating model. The differences between the experimental and simulated temperatures with the back-projected sources were smaller for the mode 4 simulations—between 1.2 and 1.6 times the experimental versus 1.4–1.7 times—but the back-projected model always produced better results. At 1.61 MHz, the simulated results were nearly the same as experimental results. At 1.7 MHz, the improvement over the uniformly radiating model was marked in all cases. Numerical results of the computer simulations are presented in table 2, and graphical results are presented in figures 3–6. Figure 3 presents acoustic field results, discussed above. Figure 4 displays peak temperature rise in terms of degrees per watt of applied acoustic power. At lower mode numbers the uniformly radiating model is very far from the experimental results, whereas the back-projection method shows good agreement at both low and high modes.

The thermal distributions measured *in vivo* with MRI are shown in figure 5. The MRI profiles were slightly wider than the simulated profiles from the uniformly radiating model, but were in fairly good agreement with the simulations produced by back projection; the areas enclosed by the contours were comparable in size to those in the MR images. Radial distributions through the focus are shown in figure 6. These temperature field profiles represent the average of all temperature fields obtained from the same experimental parameter set. In both

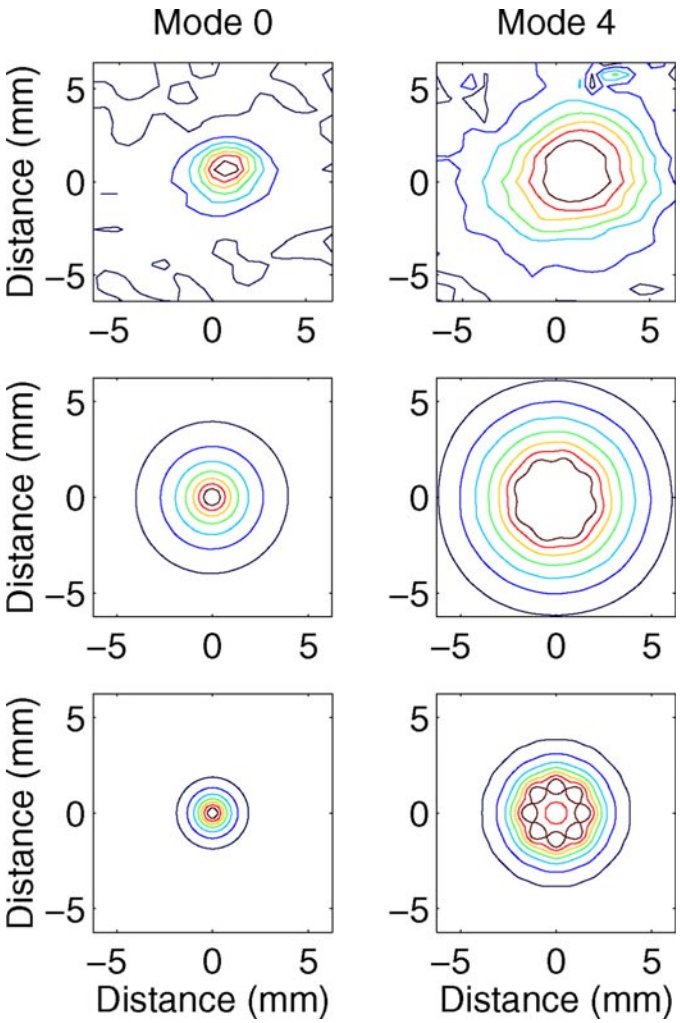

Figure 5. MRI measured (top), back-projection simulated (middle) and uniformly radiating simulated (bottom) temperature distributions from a plane through the focus for different operating modes of the 1.61 MHz transducer. The lines are contours at 10% intervals and each plot is normalized by its peak value. (Peak values can be found in table 2.) The temperature elevation shown is after a 10 second pulse from the 1.61 MHz transducer. The resolution of the experimental (MRI) distributions is 0.64 mm; it is 0.1 mm for the simulated distributions.

cases, the experimental temperature profiles were wider and flatter than the uniformly radiating simulated profiles but were close to the back-projection simulated profiles.

4. Discussions and conclusions

While we saw excellent agreement between theoretical and measured acoustic fields in water, the temperature fields in tissue were wider than those predicted by theory when a uniformly radiating transducer was assumed, and the experimental peak temperature values were lower by a factor of approximately two. Our MRI temperature measurements (mode 0) are comparable to the published value of 1.3 $^{\circ}$C W^{-1} that was measured using an invasive microthermocouple

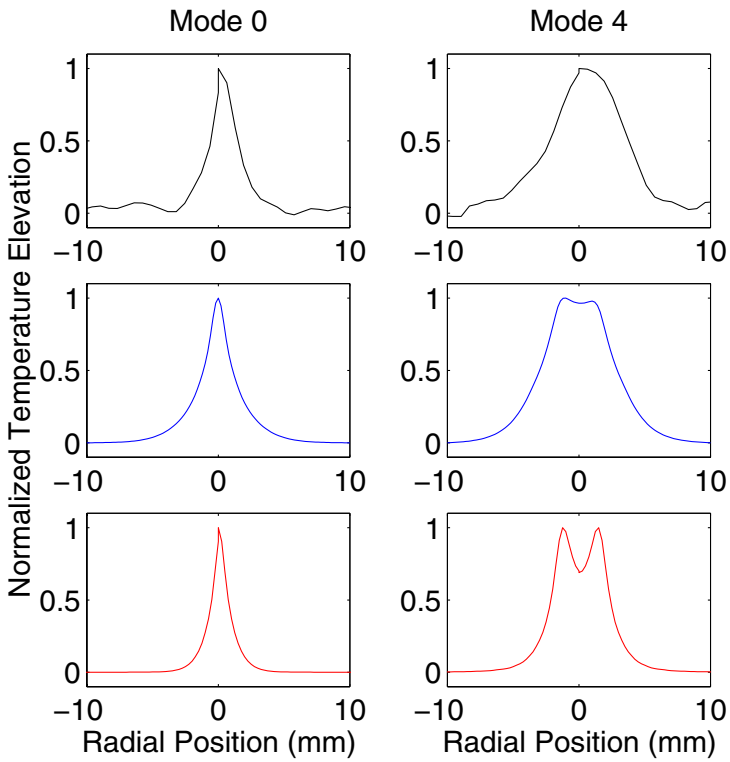

Figure 6. Comparison of experimental (MRI, top row), back-projection simulated (middle row) and uniformly radiating simulated (bottom row) temperature elevation profiles for modes 0 and 4 after 10 second sonications. Notice that the experimental and back-projection simulated profiles are slightly wider than the uniformly radiating simulated profiles, but are in good agreement with each other. These results are for the 1.61 MHz transducer. MRI results are the average of multiple sonications.

in rabbit thigh muscle *in vivo* (Hynynen *et al* 1996) during sonication with a single focus transducer ($R = 8$ cm, $D = 10$ cm, $f = 1.5$ MHz). Thus the discrepancy between the experimental and theoretical results must arise from inadequacies in the numerical model.

Nonlinear effects were not taken into account in our models, because it has been shown (Swindell 1985, Hynynen 1991) that nonlinear effects result in only a small enhancement in heating observed with the sharply focused transducers used in this study. This was tested using the model developed by Hallaj *et al* (2001). The calculated increase caused by nonlinear propagation was 0.041 $^{\circ}$C W^{-1}. The effects of thermal lensing (Le Floch and Fink 1997, Simon *et al* 1997) were likewise not expected to be significant under our experimental conditions (10–20 s pulse length, no substantial fatty layers) (Hallaj *et al* 2001). However, the effects of scattering of the ultrasound beam by tissue inhomogeneities may account for some of the differences from theory. The attenuation and absorption coefficients have been taken to be the same; attenuation in our model was assumed to result only from the ultrasound being absorbed by the tissue, not from interfacial reflections or scattering of the beam. The model also assumed two homogenous layers with interfaces parallel to the transducer face. While reflection from a water–tissue or tissue–tissue interfaces is small ($<1\%$, based on impedance calculations) for normal incidence, it increases as the angle deviates from normal.

In addition, tissue is not homogenous: muscles have fibres, blood vessels, interfaces and fat pockets, which may distort or deflect the ultrasound beam: the effects of muscle fibers on sound speed are known. For example, the speed of sound in muscle depends upon the direction of propagation (Duck 1990); it is faster along the fibers than across. Similar variations in attenuation/absorption are also not taken into account, nor are any changes in the values of these properties with temperature accounted for. Broad based scattering in the fine structure of the tissue could result in overall smearing of the focus: the temperature profile would widen and the sharp peaks would be flattened out, but the overall energy deposited would not be significantly lessened. These scattering effects could thus result in good agreement between predicted and observed lesion sizes. The fact that the disagreement between theory and experiment was less in our experiments in the higher modes where the focus is already larger lends some support to this argument.

However, transducer nonuniformity clearly accounted for the majority of the differences between simulated and experimental temperature fields, as our second set of simulations—which made use of experimental characterizations of the transducers in the simulation process—showed. By directly measuring the pressure field generated by a particular transducer, a realistic source distribution, and consequently a much more accurate prediction of the pressure and temperature fields in tissue, can be obtained from simulations.

Another source of error in the temperature prediction is the bioheat equation. While it models thermal conduction accurately, it only approximates the effects of blood perfusion. It does not take into account convective heat transfer by large (diameter > 0.3 mm) blood vessels. Fortunately, the heat conduction effects dominate during short sonications (Billard *et al* 1990), and thus the error in approximating the perfusion effects does not have a major effect during short ultrasound exposures. However, the large blood vessels would still have a significant effect on the temperature elevation for short sonications (Dorr and Hynynen 1992, Kolios *et al* 1996).

The nearly real-time feedback provided by MRI makes it possible to observe over or undertreament after each sonication. When the number of parameters to be adjusted is few, as with a single focus transducer which allows only for the varying of power, duration and position, modifications of the parameters during the treatment could, in principle, even be done by the operator. With a phased array, both the amplitude and phase of each element can be controlled independently, and consequently the number of parameters to adjust becomes too high for manual adjustment. Consequently, good treatment planning is important with phased arrays (Daum *et al* 1999). Up until now simulations have relied on the uniformly radiating model for determining the source distributions, and these models have produced peak temperature values which are too high, especially in the single focus (or mode 0) case. This discrepancy is better but still not acceptable when the focal volume is increased by a phased array. Based on our results, this discrepancy appears to mainly arise from the fact that transducers are not ideal and uniformly radiating and produce distorted pressure fields. By experimentally measuring the pressure field of the transducer, a characteristic fingerprint of the transducer is obtained. In a similar but more *ad hoc* approach, Fan *et al* (1997) proposed a method for measuring the acoustic field produced by a single source transducer and using inverse techniques to model the equivalent phased array excitation source. This data obtained in a water tank can be back-propagated to the transducer face and then forward-propagated through tissue to obtain, ultimately, a predicted temperature field, which will yield better agreement with experimental results. Our results demonstrate a better way to plan focused ultrasound treatments and indicate the importance of using real, measured data in the temperature prediction models. Furthermore, since the measurement plane does not need to be at the focus, the fields can be measured at the actual treatment powers.

Acknowledgments

This work was supported by NIH grant CA46627 and a CIMIT grant and equipment supplied by TxSonics, Inc. (Haifa, Israel).

References

Billard B E, Hynynen K and Roemer R B 1990 Effects of physical parameters on high temperature ultrasound hyperthermia *Ultrasound Med. Biol.* **16** 409–20

Cain C A and Umemura S-I 1986 Concentric-ring and sector-vortex phased-array applicators for ultrasound hyperthermia *IEEE Trans. Microwave Theory Tech.* **34** 542–51

Carstensen E L, Becroft S A, Law W K and Barber D B 1981 Finite amplitude effects on thresholds for lesion production in tissues by unfocused ultrasound *J. Acoust. Soc. Am.* **70** 302–9

Chung A, Hynynen K, Cline H E and Jolesz F A 1996 Quantification of thermal exposure using proton resonance frequency shift *Proc. SMR 4th Meeting* vol 3, p 1751

Clarke R L and ter Haar G R 1997 Temperature rise recorded during lesion formation by high-intensity focused ultrasound *Ultrasound Med. Biol.* **23** 299–306

Clement G T and Hynynen K 2000 Field characterization of therapeutic ultrasound phased arrays through forward and backward planar projection *J. Acoust. Soc. Am.* **108** 441–6

Clement G T, Liu R, Letcher S V and Stepanishen P R 1998 Forward projection of transient signals obtained from a fiber-optic pressure sensor *J. Acoust. Soc. Am.* **104** 1266

Damianou C A, Hynynen K and Xiaobing F 1995 Evaluation of accuracy of a theoretical model for predicting the necrosed tissue volume during focused ultrasound surgery *IEEE Trans. Ultrason. Ferroelectr. Freq. Control* **42** 182

Daum D R, Buchanan M T, Fjield T and Hynynen K 1998 Design and evaluation of a feedback based phased array system for ultrasound surgery *IEEE Trans. Ultrason. Ferroelectr. Freq. Control* **45** 431–8

Daum D R, Smith N B, King R L and Hynynen K 1999 *In vivo* demonstration of noninvasive thermal surgery of the liver and kidney using an ultrasonic phased array *Ultrasound Med. Biol.* **25** 1087–98

Dorr L N and Hynynen K 1992 The effects of tissue heterogeneities and large blood vessels on the thermal exposure induced by short high-power ultrasound pulses *Int. J. Hyperth.* **8** 45–59

Duck F A 1990 Thermal properties of tissue *Physical Properties of Tissue* (London: Academic)

Fan X and Hynynen K 1995 Control of the necrosed tissue volume during noninvasive ultrasound surgery using a 16-element phased array *Med. Phys.* **22** 297–306

Fan X, Moros E G and Straube W L 1997 Acoustic field prediction for a single planar continuous-wave source using an equivalent phased array method *J. Acoust. Soc. Am.* **102** 2734–41

Hallaj I M, Cleveland R O and Hynynen K 2001 Simulations of the thermoacoustic lens effect during focused ultrasound surgery *J. Acoust. Soc. Am.* **109** 2245–53

Hill C R, Rivens I, Vaughan M G and ter Haar G R 1994 Lesion development in focused ultrasound surgery: a general model *Ultrasound Med. Biol.* **20** 259–69

Hynynen K 1990 Biophysics and technology of ultrasound hyperthermia *Methods of External Hyperthermic Heating* ed M Gautherie (Berlin: Springer)

——1991 The role of nonlinear ultrasound propagation during hyperthermia treatments *Med. Phys.* **18** 1156–63

Hynynen K, Freund W R, Cline H E, Chung A H, Watkins R D, Vetro J P and Jolesz F A 1996 A clinical noninvasive MRI monitored ultrasound surgery method *RadioGraphics* **16** 185–95

Kolios M C, Sherar M D and Hunt J W 1996 Blood flow cooling and ultrasonic lesion formation *Med. Phys.* **23** 1287–98

Kuroda K, Chung A H, Hynynen K and Jolesz F A 1998 Calibration of water proton chemical shift with temperature for noninvasive temperature imaging during focused ultrasound surgery *J. Magn. Reson. Imaging* **8** 175–81

Le Floch C and Fink M 1997 Ultrasonic mapping of temperature in hyperthermia: the thermal lens effect *1997 IEEE Ultrasonics Symp. Proc. Int. Symp.* Catalogue No 97CH36118, p 1301

Lin W L, Roemer R B, Moros E G and Hynynen K 1992 Optimization of temperature distributions in scanned, focused ultrasound hyperthermia *Int. J. Hyperth.* **8** 61–78

Lizzi F L, Coleman D J, Driller J, Ostromogilsky M, Chang S and Greenall P 1984 Ultrasonic hyperthermia for opthalmic therapy *IEEE Trans. Son. Ultrason.* **31** 473–81

Lizzi F L, Driller J and Ostromogilsky M 1984 Thermal model for ultrasonic treatment of glaucoma *Ultrasound Med. Biol.* **10** 289–98

Meaney P M, Clarke R L, ter Haar G R and Rivens I H 1998 A 3-D finite-element model for computation of temperature profiles and regions of thermal damage during focused ultrasound surgery exposures *Ultrasound Med. Biol.* **24** 1489–99

Nyborg W L 1981 Heat generation by ultrasound in a relaxing medium *J. Acoust. Soc. Am.* **70** 310–12

Pennes H H 1948 Analysis of tissue and arterial blood temperatures in the resting human forearm *J. Appl. Physiol.* **1** 93–132

Robinson T C and Lele P P 1972 An analysis of lesion development in the brain and in plastics by high-intensity focused ultrasound at low-megahertz frequencies *J. Acoust. Soc. Am.* **51** 1333–51

Simon C, VanBaren P and Ebbini E 1997 Quantitative analysis and applications of non-invasive temperature estimation using diagnostic ultrasound *1997 IEEE Ultrasonics Symp. Proc. Int. Symp.* Catalogue No 97CH36118, p 1319

Swindell W 1985 A theoretical study of nonlinear effects with focused ultrasound in tissues: an 'acoustic Bragg peak' *Ultrasound Med. Biol.* **11** 121

Swindell W, Roemer R B and Clegg S T 1982 Temperature distributions caused by dynamic scanning of focused ultrasound transducers *Proc. IEEE Ultrasonics Symp.* pp 745–9

Zemanek J 1971 Beam behavior within the nearfield of a vibrating piston *J. Acoust. Soc. Am.* **49** 181